

Multimode scanning x-ray diffraction microscopy for diamond anvil cell experiments

Rostislav Hrubciak,^{a)} Jesse S. Smith, and Guoyin Shen^{a)}

High Pressure Collaborative Access Team (HPCAT), X-ray Science Division, Argonne National Laboratory, Illinois 60439, USA

^{a)}Authors to whom correspondence should be addressed,
e-mail: hrubiak@anl.gov; and gyshen@anl.gov

We have designed and implemented a new experimental system for fast mapping of crystal structures and other structural features of materials under high pressure at the High Pressure Collaborative Access Team (HPCAT), sector 16 of the Advanced Photon Source. The system utilizes scanning X-ray diffraction microscopy (SXDM) and is optimized for use with diamond anvil cell (DAC) devices. In the SXDM, the X-ray diffraction (XRD) is collected in a forward scattering geometry from points on a two-dimensional grid by fly-scanning the sample with respect to a micro-focused X-ray beam. The recording of XRD is made during the continuous motion of the sample using a fast (millisecond) X-ray area detector in synchrony with the sample positioners, resulting in a highly efficient data collection for SDXM. A new computer program, *X-ray Diffractive Imaging* (XDI), has been developed with the SXDM system. The XDI program provides a graphical interface for constructing and displaying the SXDM images in several modes: (1) phase mapping based on structural information; (2) pressure visualization based on equation of state; (3) microstructural features mapping based on peak shape parameters; and (4) grain size and preferred-orientation based on peak shape parameters. The XDI is a standalone program and can be generally used for controlling and displaying SXDM images at other places. Two examples of iron and zirconium samples under high pressure are presented to demonstrate the applications of the SXDM.

PACS numbers: 07.35.+k, 07.85.Tt, 07.85.Qe

Keywords: diamond anvil cell, synchrotron x-ray diffraction, x-ray microscopy

I. INTRODUCTION

Materials subjected to various high pressure (P) and high/low temperature (T) treatments in the diamond anvil cell (DAC)^{1,2} often exhibit a large degree of complexity and inhomogeneity, on length scales ranging from nanometers to hundreds of microns. An ability to perform fast and detailed spatially resolved characterizations of the inhomogeneity under high pressure, or in the high P - T treated samples, has great promises to unlock the complexity and to gain understanding of a multitude of emerging physical phenomena in high pressure sciences²⁻⁸.

In-situ X-ray diffraction (XRD) at synchrotron beamlines has been widely used to characterize important materials properties, such as crystal structure, unit cell dimensions, polymorph fractionation, grain size, texture (preferred grain orientations), anisotropic strain, pressure gradient, etc. Obtaining information about the inhomogeneity of samples in a DAC involves manually collecting and analyzing the XRD data at a multiple set of chosen points, e.g., 2-dimensional (2D) grid, across a sample volume of interest^{3-5,8}. Due to the geometry of the DAC system, the samples are typically thin in the dimension along the X-ray beam and thus 2D imaging, as opposed to 3D, is often adequate. Spatially resolved high- P data collected in this way could be reduced with software, such as Fit2D⁹, Dioptas¹⁰, GSAS¹¹, GSAS-II¹² or GSE_ADA¹³, and then displayed in

2D, as an image, using other custom software scripts devised by the individual experimenters^{3-5,8}. This kind of data collection and analysis can be challenging and time consuming due to specialized nature of each high- P experiment. Meanwhile, some other areas of research, e.g., in materials and biological sciences, have recently benefitted from the development of X-ray diffraction microscopy (SXDM) systems that can perform spatially-resolved X-ray diffraction data collection and visualization with greatly improved levels of automation^{14,15,24-29,16-23}.

High Pressure Collaborative Access Team (HPCAT) is a facility at the Advanced Photon Source (APS) that hosts hundreds of visiting users each year who routinely make use of the DAC devices with *in-situ* XRD for study of materials under high P - T conditions; therefore, the scope of this work is to establish a dedicated XRD microscopy system, optimized for fast 2D visualization of complexities in materials during high- P experiments, particularly in a DAC. We have designed and implemented such a SXDM system for high- P experiments at the HPCAT beamlines 16-ID-B³⁰, 16-BM-B⁸, and 16-BM-D³¹, at the APS. The system, as described here, is currently available for user operation.

II. SYSTEM DESIGN

A. Design objectives and features

Visiting users come from a broad range of backgrounds and are interested in characterizing a wide variety of materials properties in a DAC. Therefore, the SXDM system should be general enough to accommodate as many modes of materials' complexity visualization as possible. At the same time, the system should be focused on a few common tasks to improve efficiency and to simplify applications for users with minimal training. With these considerations, together with the geometry of a typical DAC, the system was designed to have the following features:

- 1 μm or better spatial resolution – achievable with existing sample positioners and X-ray beam focusing optics³²
- Fast 2D mapping based on structural feature(s) – crystal structure contrast, phase mapping
- Fast pressure visualization based on equation of state (EOS) – mapping the pressure/stress distribution on the sample chamber
- Fast microstructure visualization – mapping grain size, preferred orientation, and differential strain based on texture and peak broadening
- Composite image creation – 2D visualization of multi-phase systems, new phase identification
- Modular data acquisition and visualization – data visualization program is portable; users may install the visualization software on their own computers and continue data visualization/analysis post experiment
- User friendly – easy to operate

In the SXDM system described here, the sample is 'fly-scanned' in a rectangular grid pattern with respect to a focused X-ray probe³². Both the X-ray transmission signal and the XRD images are recorded simultaneously, using a small diode integrated to the X-ray beam-stop and a fast X-ray area detector, respectively. Multiple modes of 2D visualizations, depending on the experimental goals, are made possible with a newly developed computer program, X-ray Diffractive Imaging (XDI), described below.

B. SXDM for high- P experiments

The diffracted X-ray photon counts in the XRD patterns encode the structure factor of the X-ray scattering material, a function $I(\vec{q})$, where \vec{q} is the momentum transfer vector, related by the Bragg law to the 2θ and the azimuthal (φ) angles of the scattered X-rays. The structure factor, $I(\vec{q})$, is sensitive to structures in the material that are on a continuum of length scale – from the atomic level to the cross-sectional size of the X-ray probe. Therefore, $I(\vec{q})$ may be influenced by a multitude of extrinsic and intrinsic characteristics of a material, e.g., crystal structure, strain, preferred orientation (i.e., texture), grain-sizes, temperature, pressure. Visualization of complexity in materials properties may consequently be accomplished by displaying in 2D the values of some appropriate functional, $F(I)$, that is sensitive to a particular observable property. The corresponding $F(I)$ can be computed directly from the measured XRD patterns. An obvious example of $F(I)$ is a definite integral of the form:

$$F(I) = \int_{q_0}^{q_1} I(q) dq \quad (1)$$

Here, $F(I)$ may be a diffraction peak, or a few peaks, of a given phase or a section of structural features. This type of functional is sensitive to the amount of the corresponding polymorph, or phase, in the X-ray probe's cross section and may be used to visualize the crystalline structure variations in a sample. In this case, the $F(I)$ is computed by integrating X-ray counts from a narrow q region surrounding a specific hkl reflection of some phase of the material (**Error! Reference source not found.**).

Other functionals may be computed from the observed XRD patterns that are sensitive to other corresponding materials properties. As described in subsequent sections, these functionals may include the extracted shape parameters of specific diffracted peaks (e.g., $2-\theta$ value at peak center, peak spread, peaks' relative amplitudes, φ -angle preferred orientation of peaks). A new computer program, XDI, creates in computer memory a data structure, which contains $I(q)$ for each of the measured XRD patterns. Storing the entire set of $I(q)$ points in memory is advantageous, so that the subsequent selection of a type of $F(I)$, sensitive to some material property, and the visualization of its spatial distribution can be performed in a timely manner.

C. Data collection

The data collection system used to generate the 2D grid of XRD images is an extension of HPCAT's basic sample scanning system³². A typical DAC sample chamber has a diameter ranging from a few microns to a few hundred microns and, in most cases, it is confined by a metallic gasket (e.g., FIG. 4A). To locate the sample chamber with respect to the x-ray beam the DAC is systematically scanned in the plane normal to the x-ray beam³³. HPCAT has developed the ability to scan samples 'on the fly.' This has been crucial in the complementary development of SXDM as it significantly reduces the time required to generate a 2D grid of x-ray images³². The motion and triggering process used for the x-ray transmission scan is simultaneously used to trigger a high-frequency, photon-counting (shutterless) area detector (Pilatus 1MF) for collecting XRD data for subsequent analysis in XDI.

The simultaneous x-ray transmission/diffraction scans are carried out at beamline 16-ID-B at the APS. A more detailed description of the beamline's source and front-end optics can be found elsewhere³⁰. Here, we briefly note that using an undulator with tunable gap and a Si double-crystal monochromator, users can select monochromatic beam ranging in energy from 18-60 keV. At a typical operating energy of 30 keV using the Si (111) crystal pair the flux on the sample is on the order of 10^{11} photons/sec.

Focusing optics include a choice between two Kirkpatrick-Baez mirror assemblies. The large-mirror assembly includes a pair of 320-mm mirrors and can focus the beam to better than $4\ \mu\text{m}$ (vertical) \times $7\ \mu\text{m}$ (horizontal) as characterized by the full-width-at-half-maximum (FWHM) of the derivative of a knife-edge scan. The small-mirror assembly includes 200-mm and 100-mm mirrors for focusing in the vertical and horizontal directions, respectively. It can focus to better than $1\ \mu\text{m}$ (vertical) \times $2.5\ \mu\text{m}$ (horizontal). This improvement in spatial resolution comes at the cost of flux—about 20% of that obtained with the large-mirror assembly³².

A dedicated graphical user interface, called *Diptera*, has been developed for defining, executing, and displaying the data from 1- and 2-D flyscans³². *Diptera* allows x-ray images to be simultaneously collected with x-ray transmission data, with same dimension, step size, and count time as defined in the *Scan Control* panel. These images are input into XDI for extended analysis.

Typical dimensions of the 2D flyscans are of the order of 20x20 to 100x100 points. Constructing SXDM images with larger dimensions is possible; however, dimensions higher than 100x100 points have not yet been used routinely for high pressure samples.

D. Data visualization

The data visualization is done using the graphical XDI program. XDI makes use of the LabVIEW³⁴ graphical programming infrastructure, which provides the necessary flexibility for designing the graphical user interface (GUI).

1. User interface

The XDI contains a graphical interface of the workflow steps for generating SXDM images given a set XRD patterns that were acquired previously in 2D flyscans, as described in the Data collection section above. The main window of the XDI GUI is shown in FIG. 2, with the left side of the window displaying XRD patterns and the right side displaying the SXDM images.

The XDI GUI contains elements for various tasks that are useful for constructing and examining SXDM images (some of the tasks are described with more detail in later subsections):

(1) *Menu strip options*. “File” menu is used for opening XRD files, saving and loading projects, exporting re-binned and integrated XRD files; “Setup” menu contains shortcuts to XRD geometry calibration, XRD pattern masking, and region of interest (ROI) creation modules; “Imaging” menu contains shortcuts to tasks related creating, saving and loading a data structure, which contains an $I(q)$, calculated from each of the measured XRD patterns.

(3) *XRD pattern pane*. The left side of the XDI window can be toggled to display either a raw XRD pattern or the corresponding XRD pattern re-binned to a radial (2θ vs. φ) coordinate system. Options for customizing various elements of the XRD pattern pane are available from right-click pop-up menus.

(4) *Integration/2-D grid pane*. The right-hand side of the XDI window can be toggled between *integration* and *2D grid view* tabs. The *integration* tab displays an integrated XRD pattern corresponding to the XRD pattern currently displayed in the *XRD pattern pane*. This tab contains tools for examining the integrated XRD patterns, phase identification, and determining pressure. The *2D grid view* displays the SXDM images based on the $I(q)$ data structure currently in memory in conjunction with user settings selections (described below). Clicking anywhere on the SXDM image, or using the keyboard arrow keys, will move the SXDM image cursor to the selected location and display the corresponding XRD pattern in the *XRD pattern pane*. Bi-linear interpolated SXDM images are displayed by default, although the interpolation can be toggled off to display raw SXDM voxels. Right-hand side of the *2D grid view pane* contains display customization options, such as cursor, overlays, scale bar, interpolation, intensity scaling, as well

as several shortcuts to related to a GUI module for composite image creation (described below). A right-click pop-up menu allows selection of different color tables for drawing the SDXD images.

The lower part of the *2D grid view pane* contains selection tabs for various modes of constructing the SXDM images (described in greater detail in later subsections): “All peaks” tab provides functionality for automatic phase identification based on observed XRD peaks; “ 2θ ” tab contains a GUI for manual selection of q -space contrast (i.e., given the functional in EQ.1); “ROI” tab contains options for selective integration of XRD counts encompassed by user-specified arbitrary geometric regions of interest in the XRD patterns; “Peak fit” tab is used for constructing SXDM images based on XRD peak shape parameters contrast (e.g., d -spacing, amplitude, spread); “Pressure” tab is used to obtain pressure maps based on known EOS(s).

2. Automated data reduction

As parts of the workflow for SXDM image creation, XDI contains graphical sub-modules that enable to create in memory the data structure containing the $I(q)$ from the collected grid of XRD patterns. These modules include:

- (1) *XRD geometry calibration*. The geometry calibration may be done in a fully automated mode given a calibrant XRD pattern (e.g., CeO₂, LaB₆). Full automation is enabled via calibrant diffraction circle finding using the Hough transform image search algorithm³⁵. XDI uses the geometry description convention similar to Fit2D⁹ program, which is commonly used in the high pressure community, and includes support for the newer PyFAI³⁶ / Dioptas¹⁰ type parameters.
- (2) *XRD data re-binning and reduction to $I(q)$* . XRD data dimensionality reduction is done via a Cartesian to radial geometry pixel re-binning. The re-binning functions in XDI are implemented in LabVIEW, but are based on the previously described paradigms that includes pixel-splitting³⁶, look-up table generation³⁶, masking^{9,10}, and background image subtraction^{9,10}. The accuracy of re-binning in XDI was validated by comparing outputs to other commonly used re-binning software^{9,10}. XRD pattern re-binning is a computing-intensive task, however, given the multi-core parallel processing optimization, the re-binning of a single pattern (e.g., 981 by 1043 pixels, Pilatus 1MF image file) takes 50 milliseconds or less on a personal computer (PC) with a 4-core Intel Xeon CPU E5-1607, 3.00 GHz. Therefore, a typical-resolution $I(q)$ memory structure (e.g., 31x31 points) can be generated in less than 1 minute.
- (3) *Multiple $2\theta/\varphi$ ROI's*. XDI allows to select multiple ROI's in the XRD patterns to be treated individually in the computation of $I(q)$. As is described in later sub-sections, this feature is useful for the visualization of high- P microstructure.

3. Miscellaneous features

XDI includes a GUI to some additional “helper” functions, in order to increase efficiency of the users’ data viewing and assessment during the high- P experiments. Descriptions of several additional functions are given here.

a. SXDM as a sample positioning aid

XDI may be used to identify and obtain positions of small crystals in a DAC, which are not identifiable optically nor using a X-ray transmission scan, for subsequent experimental characterization with other specialized techniques², e.g., single-crystal XRD data collection and analysis¹³. The data collection system described in subsection C, above, records the sample position coordinates metadata for each recorded XRD pattern. Similarly to systems described

previously²⁸, this enables XDI to retrieve and display the corresponding motor values for any point in the displayed SXDM image. Having the record of the motor positions for each identified crystal simplifies the task of placing the small crystals directly in the path of the X-ray probe for subsequent specialized characterization.

b. Data slice function

XDI includes the capability to display 1D Cartesian plots based on an arbitrary slice through the SXDM image (as well as peak parameter plot, and pressure map). The slice view is generated by holding down the Shift key on the keyboard and drawing a line over the displayed image using the mouse (FIG. 3).

c. Combining multiple XRD files

XDI can combine (add/average) the counts from multiple XRD files, corresponding to selected 2D portion of the sample, which can be useful for improving the signal statistics. XDI provides a convenient way to combine the counts from multiple XRD files corresponding to a contiguous region on the currently displayed SXDM image. The XRD patterns may be combined by holding down the Control key on the PC keyboard and drawing a rectangle on the SXDM image using the mouse, encompassing the points that are to be combined. The resulting XRD pattern can be saved as TIFF type file and can be used for further analysis in external software.

d. Composite image creation

XDI enables combination of multiple SXDM images (i.e., individually generated images based on various contrast functionals, as described in preceding sub-sections) into a single “false-color” composite image. In the composite image, arbitrary colors may be assigned to the “layers” that are being composited. For example, the false-color images may be used to represent qualitatively the 2D phase distribution in an Fe sample (FIG. 4).

III. SXDM MODES AND APPLICATIONS

A. Fast SXDM based on structural features: 2D high- P phase identification

As mentioned above, selective q -space contrast (i.e., given the functional in EQ.1) is one of the primary ways to visualize the spatial distribution of crystalline phases with XDI. XDI integrates XRD counts in a selected ROI of q -space for each of the collected XRD patterns and displays the result as a “heat map” 2D image. The resulting SXDM images may be used for high- P phase identification whenever user-supplied structure files are loaded. The so-called momentum transfer (q) contrast SXDM images may be drawn by XDI in either of two modes, manual or automatic 2θ ROI selection:

- (1) *Manual 2θ ROI selection*: the XRD-contrast images can be constructed quickly by graphically selecting a 2θ value and adjusting the 2θ region of interest (e.g.: clicking on the 2θ in the XRD pattern (FIG. 2A) or in the 1D $I(2\theta)$ plot (FIG. 2D); fast-adjusting the 2θ in the 1D $I(2\theta)$ using the computer mouse scroll-wheel). The selection of 2θ triggers a real-time update of the corresponding SXDM image.
- (2) *Automatic 2θ ROI selection*: Automatic 2θ selection can be done based on automatic peak searching, as well as based on the currently loaded phase information, i.e., Joint Committee on Powder Diffraction file format (JCPDS), containing a computed factor coupled with an

equation of state, commonly used in the high-pressure community. Peak search option runs a global peak search algorithm on each of the XRD patterns and generates a thumbnail SXDM images using 2θ values of all found peaks.

Metastable iron phase at high- P and 295K

Iron (Fe) metal at a P of 40GPa and at ambient temperature adopts a hexagonally-close-packed (hcp) structure. At the same P and $T > \sim 1800\text{K}$, Fe transforms to a face-centered-cubic (fcc) structure. The rapid quenching in temperature in the laser-pulse heated DAC³⁷ often allows for the high temperature phases³⁸ or microstructure³⁹ to retain their structures metastably back to room temperature. In our experiments on Fe, the sample in a DAC is subjected to a series of heating pulses with increasing laser power for each subsequent pulse, in order to survey temperature states between 1,000 and 6,000K with intervals of $\sim 10\text{-}50\text{K}$, using the experimental setup described in refs^{37,38}. SXDM analysis is performed after each laser heating pulse in order to visualize the complexity and changes in the micro-structure of the Fe sample induced by a range of P - T conditions. For example, in FIG. 4B, a false-color microstructure image shows spatial distribution of phases of Fe after pulse-heating the sample to a T above the hcp-fcc transition, and quenching rapidly to room T . Two different polymorphs of Fe, hcp and fcc, can be seen coexisting in a T -quenched sample. The XRD data for construction of the SXDM image in FIG. 4B is obtained by 2D fly-scanning the sample across a focused X-ray beam ($3 \times 5 \mu\text{m}$ FWHM), using a grid of 21×21 points with a step size of $2 \mu\text{m}$. The SXDM image (FIG. 4B) is constructed using the 2θ selection mode.

B. Pressure visualization based on EOS

The ability to resolve local pressure variations in high pressure samples provides essential stress information of the sample environment. XDI provides the capability to rapidly visualize pressure variations in samples, provided that a pressure-volume-temperature (P - V - T) EOS of the constituent phase is known. XDI calculates the unit cell volume for each XRD pattern using automated hkl peak recognition and d -spacing calculation. Volumes of the unit cell may be combined with a user-provided EOS information (e.g., JCPDS file) for a given material to generate 2D pressure-distribution images.

Unexpectedly large pressure gradients in hydrostatically compressed zirconium

Group 4 transition metals, titanium, zirconium, hafnium, take on an hcp structure (α) at ambient P , and transform to another hexagonal phase (ω) under compression. In each case, literature reports of the $\alpha \rightarrow \omega$ transition pressure are scattered and the true phase equilibrium pressure has still not been resolved⁴⁰⁻⁴⁴. 2D pressure mapping using the SXDM approach can shed light on the issue by improving the understanding of the local pressure conditions for individual grains as they undergo a phase transition. For example, an annealed multigrain Zr sample pressurized in a DAC (FIG. 5A) is used to plot a 2D pressure map (FIG. 5B). The ultra-high purity Zr sample is compressed hydrostatically in a DAC with neon as a pressure transmitting medium⁴⁵, annealed at $\sim 1000\text{K}$ for 10 minutes using laser-heating at 16-ID-B³⁷, and compressed to P at 4.5 GPa. The overall pressure of the sample chamber is determined using the ruby fluorescence method. A $1 \times 2 \mu\text{m}^2$ X-ray beam with a flyscan of 21×21 points and a step resolution of $0.5 \mu\text{m}$ is used to collect the XRD data. The resulting SXDM image (FIG. 5B) reveals remarkably large pressure gradients ($>20\%$) between neighboring Zr domains with a length scale of just a few microns. Three distinct domains are identifiable visually in the SXDM image, two light-shaded domains showing higher

P (~ 5.7 GPa) and a dark-shaded domain showing a relatively lower P (~ 4.4 GPa) in between. A possible explanation is that the internal strength of individual Zr domains coupled with specific geometric packing may allow low P domains to exist nested in between higher P domains. This new observation may shed light on the disagreements on the Zr phase boundaries existing in literature.

C. Visualizing microstructural phenomena with XRD peak shape parameters

Observable XRD peak shape parameters, such as 2θ peak center, FWHM, relative peak amplitudes and positions are sensitive to multiple microstructural phenomena, such as grain-size distribution, preferred orientation (texture) and differential strain. Indeed, combinations of these phenomena often coexist within high- P samples. Therefore, due to possibility of multiple underlying causes, the exact nature of the observed peak parameters is difficult to pinpoint using a single-point XRD. However, as exemplified below, the underlying microstructural phenomena often become immediately apparent after resolving the variations in observed XRD peak parameters in 2D. XDI supports 2D SXDM visualization based on XRD peak shape parameters in 2θ space as well as variations in a particular XRD reflection in φ space. As a result, this functionality provides a qualitative high-resolution view of the microstructural inhomogeneity and complexity in high- P samples.

Zirconium grain microstructure at high- P

In subsection 4 above, we discussed 2D mapping capabilities in XDI. Later, we provided an example of using the computed d -spacings for observed hkl peaks to generate a 2D pressure map for a Zr sample hydrostatically compressed in a DAC. Using the same dataset, here we show an SXDM visualization using the computed hkl peak widths (FWHM), rather than the d -spacings, of the observed Zr peaks. For example, FIG. 5C shows in 2D a variation of Zr (101) peak width (FWHM), with brighter shading indicating larger peak width relative to the darker shaded regions. Features that become apparent in the image, labeled “*Domain boundary*” in FIG. 5C, coincide with the boundaries between the distinct domains seen in the 2D pressure map FIG. 5B (see subsection 4, above). In this example, we observe an increase in the integrated peak width on the boundary between domains. Due to the pressure differential between the domains, when the X-ray beam is directly over the boundary, we observe a convolution in XRD of signals with different d -spacing, i.e., the broadening of the integrated peak. We note that, while single point XRD often doesn’t provide sufficient information for unambiguous interpretation of microstructural phenomena underlying the observed XRD peak parameters under high- P , the 2D SXDM technique opens a clear new insight into the microstructural state of materials. Conversely speaking, peak shape parameters may be used to visualize qualitatively the domain boundaries and other microstructural features within high- P samples, provided that an appropriate physical model is used.

D. 2D mapping of large grains

The 2D shapes of coarse grains (i.e., larger than the X-ray beam cross-section) can be visualized qualitatively in XDI. For a grainy sample, Bragg XRD coarse spot reflections can be selected individually using the ROI editing GUI in XDI. Subsequently, XDI can display in 2D a heat map of the integrated counts in the selected ROI’s. This type of SXDM image shows qualitatively the 2D shapes of the corresponding grain(s).

Coarse grains in laser-heated iron at high- P

Laser heating of iron samples in a DAC may induce localized grain growth, with individual grains growing to sizes larger than the probing X-ray beam. After turning off the heating laser, the samples are temperature-quenched, and the high- T coarse microstructure is often preserved. SXDM analysis can be used to visualize the shapes and positions of the coarse grains and correlate their positions with the position of the heating laser and/or temperature maps³⁸. FIG. 6A exemplifies a construction of an SXDM image that shows a 2D shape of a coarse grain in a Fe sample in a DAC that was laser heated to induce grain coarsening. For constructing the SXDM image in FIG. 6A, an Fe sample in a DAC at a P of 203GPa is laser heated locally with infrared lasers focused to $\sim 10\ \mu\text{m}$ FWHM using an experimental setup described in refs^{37,38}. Several coarse grains are present in the sample after the heating. When the X-ray beam is centered on a coarse grain, coarse Bragg diffraction spots are observed recorded in the XRD pattern. FIG. 6 (right) shows an XRD pattern containing a detail of a typical Bragg spot arising from one of the coarse grains. An ROI on the XRD pattern, confined to the area just around a particular Bragg spot, is specified using XDI GUI. When scanning the sample in 2D with respect to the X-ray beam, the integrated counts within the ROI are maximized whenever the X-ray beam goes through the grain and diminish whenever the beam is not incident on the grain. Subsequently, a 2D variation of the integrated intensities in the ROI can be displayed by XDI, representing qualitatively the positions of the coarse grain in the sample. A composite, false-color SXDM image, showing all identified grains may be created in XDI using the composite image creation GUI. It should be noted that due to the limitation of monochromatic XRD method, only the grains that satisfy the Bragg reflection condition (without the rotation of the sample) may be identified using this approach. On the other hand, white X-ray Laue XRD (e.g., at beamline 16-BM-B⁸) in combination with functionality of XDI, may be used to identify and map practically all of the coarse grains existing in the sample⁴⁶. Further, point-spread-function de-convolution may be applicable to SXDM images of the coarse grains in order to reduce the broadening artifact caused by the finite size of the x-ray probe.

E. Preferred-orientated microstructure

Using an approach similar to one described in subsection 6, above, highly textured (e.g., preferentially aligned or mosaic crystals) microstructure can be visualized by the use of custom ROI's in 2θ -space and/or φ -space.

Preferred orientation in laser-heated iron at high- P

Preferred bi-axial alignment of the several body-centered-cubic (bcc) metals (e.g., Mo, Mg, Fe) crystal lattice with respect to the MgO crystal substrate may be induced via a laser-heating treatment at high- P ^{38,39}. It was recently reported that Fe $P > 95$ GPa and laser-heated above the hcp-bcc transition T , while in contact with the (100)-MgO crystal surface, aligns in a preferred epitaxial orientation with respect to the MgO³⁸. After turning of the laser, a preferred oriented hcp-Fe / MgO biaxial alignment is quenched due to a topotaxial transformation from bcc to hcp Fe³⁸. The preferred alignment in hcp-Fe / MgO manifests itself in the observed XRD patterns, whereas hkl reflections of Fe and MgO are preferentially aligned axially as well as azimuthally (i.e., φ direction) (FIG. 6B top-right). SXDM imaging is used to visualize in 2D the extent of the preferred alignment in such laser-treated samples at high- P , and to correlate the alignment with the position of the heating laser spot. Appropriate ROI's are set up encompassing the observed hkl reflections maxima of Fe. Subsequently, XDI displays in 2D variations in the counts in the selected ROI's. An example in FIG. 6B (right) shows such an SXDM image of an Fe metal imbedded in single-crystal MgO that was heated above the transition T while pressurized to 203 GPa in a

DAC³⁸. A 2D scan of 21x21 points with 1 μm step resolution is done to acquire the data for the construction of the SXDM image. The blue area in FIG. 6B (right) coincides with the position of the heating lasers on the sample. SXDM analysis allows to observe the preferred bi-axial alignment of the Fe microstructure that is correlated with the laser-heating treatment.

IV. DISTRIBUTION

XDI requires a PC with a 64-bit infrastructure in order to run and has been tested on Windows 7 and Windows 10 systems. Mac OS X version may also be compiled in the future. XDI is currently available for high- P experiments at the HPCAT beamlines 16-ID-B, 16-BM-B, and 16-BM-D, at the APS. In addition, the current version of XDI is distributed free of charge via an installer download. The user base of XDI is growing and, to date, XDI has been downloaded and utilized by researchers from at least 15 different institutions. Related information may be requested from the corresponding author.

IV. CONCLUSIONS

Multimode SXDM setup described here provides a novel way to examine, in a spatially resolved manner, materials samples at high pressure conditions. Traditionally, high pressure XRD was largely considered a single-point probe. With addition of the SXDM system and XDI software, XRD can now be routinely performed as a full 2D probe. The amount of detail that can be gained from 2D has been briefly demonstrated here. However, we expect that the true potential of the technique will become apparent based on future reports of the users of this system.

ACKNOWLEDGEMENTS

The authors thank Yue Meng, Arun Bommanavar, Jeffrey Montgomery, Cheng Ji, and Dmitry Popov for helpful discussions at various stages of the development. Data on Fe was collected in collaboration with Yue Meng. Data on Zr were collected in collaboration with Changyong Park. This work was performed at HPCAT (Sector 16), Advanced Photon Source (APS), Argonne National Laboratory. HPCAT operations are supported by DOE-NNSA's Office of Experimental Sciences. The Advanced Photon Source is a U.S. Department of Energy (DOE) Office of Science User Facility operated for the DOE Office of Science by Argonne National Laboratory under Contract No. DE-AC02-06CH11357.

REFERENCES

- ¹ W.A. Bassett, Rev. Sci. Instrum. **72**, 1270 (2001).
- ² G. Shen and H.K. Mao, Reports Prog. Phys. **80**, 16101 (2017).
- ³ B. Lavina and Y. Meng, Sci. Adv. **1**, e1400260 (2015).
- ⁴ L. Wang, Y. Ding, W. Yang, W. Liu, Z. Cai, J. Kung, J. Shu, R.J. Hemley, W.L. Mao, and H. -k. Mao, Proc. Natl. Acad. Sci. **107**, 6140 (2010).
- ⁵ B. Li, C. Ji, W. Yang, J. Wang, K. Yang, R. Xu, W. Liu, Z. Cai, J. Chen, and H. Mao, Proc. Natl. Acad. Sci. 201721425 (2018).
- ⁶ O. Vidal, V. De Andrade, E. Lewin, M. Munoz, T. Parra, and S. Pascarelli, J. Metamorph.

Geol. **24**, 669 (2006).

⁷ G. Aquilanti, S. Pascarelli, O. Mathon, M. Muñoz, O. Narygina, and L. Dubrovinsky, *J. Synchrotron Radiat.* **16**, 376 (2009).

⁸ G. Shen and H.K. Mao, *Rep. Prog. Phys.* (2016).

⁹ A.P. Hammersley, S.O. Swensson, M. Hanfland, A.N. Fitch, and D. Hausermann, *High Press. Res.* **14**, 235 (1996).

¹⁰ C. Prescher and V.B. Prakapenka, *High Press. Res.* **35**, 223 (2015).

¹¹ L.A. C and V.D.R. B, *Los Alamos National Laboratory Report LAUR 86-748* (1994).

¹² B.H. Toby and R.B. Von Dreele, *J. Appl. Crystallogr.* **46**, 544 (2013).

¹³ P. Dera, K. Zhuravlev, V. Prakapenka, M.L. Rivers, G.J. Finkelstein, O. Grubor-Urosevic, O. Tschauer, S.M. Clark, and R.T. Downs, *High Press. Res.* **33**, 466 (2013).

¹⁴ H.F. Poulsen, *Mater. Res.* (2004).

¹⁵ P. Thibault, M. Dierolf, M. Andreas, B. Oliver, D. Christian, and F. Pfeiffer, *Science* **321**, 379 (2008).

¹⁶ G. Johnson, A. King, M.G. Honnicke, J. Marrow, and W. Ludwig, *J. Appl. Crystallogr.* **41**, 310 (2008).

¹⁷ O. Bunk, M. Bech, T.H. Jensen, R. Feidenhans'l, T. Binderup, A. Menzel, and F. Pfeiffer, *New J. Phys.* **11**, (2009).

¹⁸ J.-D. Grunwaldt and C.G. Schroer, *Chem. Soc. Rev.* **39**, 4741 (2010).

¹⁹ P. Thibault and V. Elser, *Annu. Rev. Condens. Matter Phys.* **1**, 237 (2010).

²⁰ C.G. Schroer, P. Boye, J.M. Feldkamp, J. Patommel, A. Schropp, D. Samberg, S. Stephan, M. Burghammer, S. Schöder, C. Riekel, B. Lengeler, G. Falkenberg, G. Wellenreuther, M. Kuhlmann, R. Frahm, D. Lützenkirchen-Hecht, and W.H. Schroeder, *Acta Phys. Pol. A* **117**, 357 (2010).

²¹ R. Falcone, C. Jacobsen, J. Kirz, S. Marchesini, D. Shapiro, and J. Spence, *Contemp. Phys.* **52**, 293 (2011).

²² B. Abbey, F. Hofmann, J. Belnoue, A. Rack, R. Tucoulou, G. Hughes, S. Eve, and A.M. Korsunsky, *Scr. Mater.* **64**, 884 (2011).

²³ D. Altamura, R. Lassandro, F.A. Vittoria, L. De Caro, D. Siliqi, M. Ladisa, and C. Giannini, *J. Appl. Crystallogr.* **45**, 869 (2012).

²⁴ B. Abbey, *Jom* **65**, 1183 (2013).

²⁵ C. Giannini, D. Siliqi, M. Ladisa, D. Altamura, A. Diaz, A. Beraudi, T. Sibillano, L. De Caro, S. Stea, F. Baruffaldi, and O. Bunk, *J. Appl. Crystallogr.* **47**, 110 (2014).

²⁶ D. Siliqi, L. De Caro, M. Ladisa, F. Scattarella, A. Mazzone, D. Altamura, T. Sibillano, and C. Giannini, *J. Appl. Crystallogr.* **49**, 1107 (2016).

²⁷ M.W.M. Jones, N.W. Phillips, G.A. Van Riessen, B. Abbey, D.J. Vine, Y.S.G. Nashed, S.T. Mudie, N. Afshar, R. Kirkham, B. Chen, E. Balaur, and M.D. De Jonge, *J. Synchrotron Radiat.* **23**, 1151 (2016).

²⁸ J.A. Wojdyla, E. Panepucci, I. Martiel, S. Ebner, C.Y. Huang, M. Caffrey, O. Bunk, and M. Wang, *J. Appl. Crystallogr.* **49**, 944 (2016).

²⁹ J.D. Nicolas, M. Bernhardt, A. Markus, F. Alves, M. Burghammer, and T. Salditt, *J.*

Synchrotron Radiat. **24**, 1163 (2017).

³⁰ J.S. Smith, S. V. Sinogeikin, C. Lin, E. Rod, L. Bai, and G. Shen, Rev. Sci. Instrum. **86**, (2015).

³¹ C. Park, D. Popov, D. Ikuta, C. Lin, C. Kenney-Benson, E. Rod, A. Bommananvar, and G. Shen, Rev. Sci. Instrum. **86**, (2015).

³² J.S. Smith, E.A. Rod, and G. Shen, *Fly Scan Apparatus for High Pressure Research Using Diamond Anvil Cells (Submitted to Rev. Sci. Instrum.)* (2018).

³³ J.S. Smith and S. Desgreniers, J. Synchrotron Radiat. **16**, 83 (2008).

³⁴ C. Elliott, V. Vijayakumar, W. Zink, and R. Hansen, J. Lab. Autom. **12**, 17 (2007).

³⁵ R. Fisker, H.F. Poulsen, J. Schou, J.M. Carstensen, and S. Garbe, J. Appl. Crystallogr. **31**, 647 (1998).

³⁶ G. Ashiotis, A. Deschildre, Z. Nawaz, J.P. Wright, D. Karkoulis, F.E. Picca, and J. Kieffer, J. Appl. Crystallogr. **48**, 510 (2015).

³⁷ Y. Meng, R. Hrubiak, E. Rod, R. Boehler, and G. Shen, Rev. Sci. Instrum. **86**, 072201 (2015).

³⁸ R. Hrubiak, Y. Meng, and G. Shen, *ArXiv:1804.05109 [Physics.Geo-Ph]* (2018).

³⁹ R. Hrubiak, Y. Meng, and G. Shen, Nat. Commun. **8**, 14562 (2017).

⁴⁰ R. Hrubiak, V. Drozd, A. Karbasi, and S.K. Saxena, J. Appl. Phys. **111**, 112612 (2012).

⁴¹ K.K. Pandey, J. Gyanchandani, M. Somayazulu, G.K. Dey, S.M. Sharma, and S.K. Sikka, J. Appl. Phys. **115**, (2014).

⁴² J. Zhang, Y. Zhao, C. Pantea, J. Qian, L.L. Daemen, P.A. Rigg, R.S. Hixson, C.W. Greeff, G.T. Gray, Y. Yang, L. Wang, Y. Wang, and T. Uchida, J. Phys. Chem. Solids **66**, 1213 (2005).

⁴³ M.K. Jacobsen, N. Velisavljevic, Y. Kono, C. Park, and C. Kenney-Benson, Phys. Rev. B **95**, 1 (2017).

⁴⁴ M.T. Pérez-Prado, A.A. Gimazov, O.A. Ruano, M.E. Kassner, and A.P. Zhilyaev, Scr. Mater. **58**, 219 (2008).

⁴⁵ M. Rivers, V. Prakapenka, A. Kubo, C. Pullins, C. Holl, and S. Jacobsen, High Press. Res. **28**, 273 (2008).

⁴⁶ D. Popov, N. Velisavljevic, W. Liu, R. Hrubiak, C. Park, and G. Shen, *Experimental Observation of Pressure Induced Grain Enlargement in Zr (in Preparation)* (2018).

⁴⁷ J. Zhang, Y. Zhao, R.S. Hixson, G.T.G. Iii, L. Wang, G.T. Gray, L. Wang, W. Utsumi, S. Hiroyuki, and H. Takanori, Phys. Rev. B **78**, 1 (2008).

Figures captions

FIG. 1. Schematic flow chart showing example steps for SXDM visualization. **A.** Schematic showing a Cartesian grid overlaying a material sample (blue). Each point on the grid represents a location for measured XRD patterns relative to the sample; **B.** Schematic showing an array of corresponding XRD patterns; **C.** Schematic showing an array of $I(q)$ computed by XDI from the measured XRD patterns, and stored in computer memory; **D.** An SXDM image drawn by XDI using the functional mode in EQ.1 with some chosen 2θ integral limits; the shape of the sample is accurately reproduced, although an additional complexity is revealed.

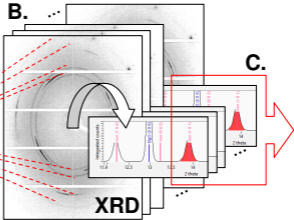
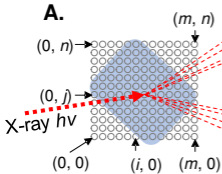
FIG. 2. XDI GUI. **A.** *XRD pattern pane*, displaying an XRD pattern, corresponding to the location selected in **B.**; **B.** *2D grid view pane*, showing an SXDM image based on a q -space (2θ) ROI selectivity mode, i.e., using the functional in EQ.1; buttons to the right allow to customize elements of the SXDM image display; **C.** Row of tab selection buttons for selecting modes of constructing the SXDM images; **D.** “Scrollable” integrated XRD $I(2\theta)$ plot, corresponding to the XRD pattern displayed in **A.**, used for selecting the q -space (2θ) integration limits.

FIG. 3. Data slice function. Left: SXDM image; right: intensity values taken from the SXDM image corresponding to the data slice path (vertical axis: counts; horizontal axis: spatial dimension).

FIG. 4. Optical microscope image of an Fe sample in a DAC (left) and a corresponding SXDM composite image (right). In this example, the SXDM image is constructed based on q -space (2θ) selectivity mode. This mode of constructing the SXDM is sensitive to the different structure polymorphs (hcp-Fe and fcc-Fe) that coexist in the sample. $P=42.5\text{GPa}$.

FIG. 5. High resolution pressure and stress visualization in hcp-Zr. **A.** Optical microscope image of a Zr sample, pressurized in a DAC; pressure measured by ruby fluorescence; **B.** SXDM image showing 2D pressure gradient; pressure calculated based on Zr(101) hkl peak d -spacing and a Zr PV EOS⁴⁷; significant variations in pressure (or strains in Zr) can be seen; **C.** SXDM images showing Zr(101) hkl peak width broadening at a domain boundary, with features less than 1 μm in size resolved by the SXDM analysis.

FIG. 6. Visualization of microstructure in a laser heated Fe sample in a DAC. **A.** Left: sharp Bragg reflection peak observed in an XRD pattern; middle: magnified portion of the XRD pattern showing the detail of the Bragg spot, and the ROI used for counts integration; right: visualized corresponding Fe coarse grain in the sample; **B.** Left: SXDM image showing local bi-axial alignment of the hcp-Fe microstructure; right: 2θ vs. φ re-binned XRD detail corresponding to points inside (top) and outside (bottom) of a laser-heated area. Laser-heater area of the Fe sample shows preferred alignment of hkl reflections with respect to the MgO reflection in φ direction (i.e., bi-axial alignment), whereas points outside the laser-heated area show no bi-axial alignment.



Open...

Previous

Next

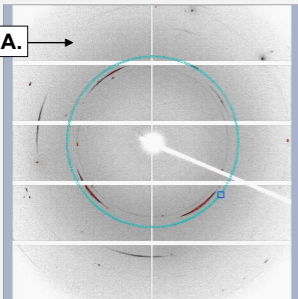
File list

Show in explorer

A

Log

A.



x: 0 y: 0 t: 0

x: 791 y: 374 t: 139

Image

20 : ϕ

P1-scan_201_0010.tif

exposure time (s) 0.997

Integration

2-D Grid

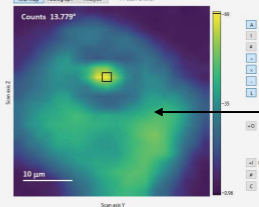
XRD map

Radiograph

Analysis

P1-scan-bhurd

Counts 13.779*



y: 0.3563 z: -0.0370 t: 2.5238 y: 0.3582 z: -0.0410 t: 56.1947

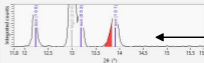
All peaks

20

ROI

Peak fit

Pressure

2 θ : 20.477 Q: 5.493 d: 1.644
q: 96.9282 θ : 13.779 Q: 3.707 d: 2.695
q: 142.334

B.

C.

D.

hcp-Fe (101)

Data slice

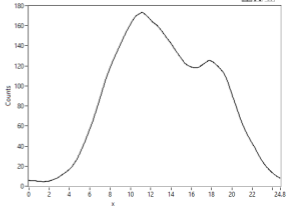
10 μm

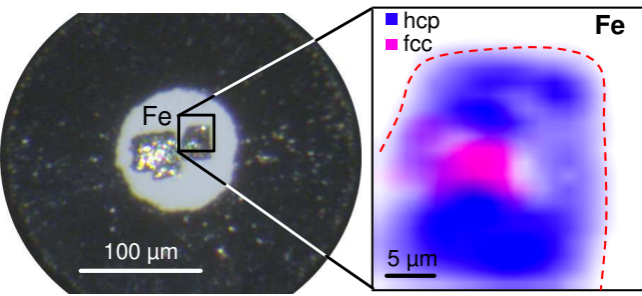
Counts
180

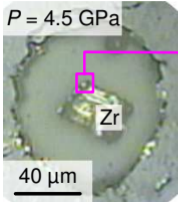
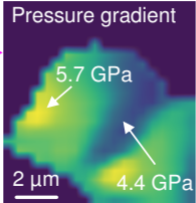
4

Slice display

Save as...





A.**B.****C.**